

# Estimation of affine transformations directly from tomographic projections in two and three dimensions

René Mooser · Fredrik Forsberg · Erwin Hack ·  
Gábor Székely · Urs Sennhauser

Received: 30 April 2011 / Revised: 5 August 2011 / Accepted: 26 September 2011 / Published online: 18 October 2011  
© Springer-Verlag 2011

**Abstract** This paper presents a new approach to estimate two- and three-dimensional affine transformations from tomographic projections. Instead of estimating the deformation from the reconstructed data, we introduce a method which works directly in the projection domain, using parallel and fan beam projection geometries. We show that any affine deformation can be analytically compensated, and we develop an efficient multiscale estimation framework based on the normalized cross correlation. The accuracy of the approach is verified using simulated and experimental data, and we demonstrate that the new method needs less projection angles and has a much lower computational complexity as compared to approaches based on the standard reconstruction techniques.

**Keywords** Computed tomography · Tomographic projections · Motion estimation

---

R. Mooser (✉) · E. Hack · U. Sennhauser  
Electronic/Metrology/Reliability Laboratory, Swiss Federal  
Laboratories for Materials Testing and Research (EMPA),  
Ueberlandstr. 129, 8600 Dübendorf, Switzerland  
e-mail: rene.mooser@gmail.com

*Present Address:*

R. Mooser  
swissQuant Group AG, Kuttelgasse 7, 8001 Zurich, Switzerland

F. Forsberg  
Division of Experimental Mechanics,  
Luleå University of Technology, 97187 Luleå, Sweden

*Present Address:*

F. Forsberg  
LKAB R&D, P.O. Box 952, 97128 Luleå, Sweden

G. Székely  
Computer Vision Laboratory, ETH Zurich,  
Sternwartstr. 7, 8092 Zurich, Switzerland

## 1 Introduction

Since its invention in the late 1960s, computed tomography (CT) is nowadays an indispensable imaging technology in medicine, non-destructive testing and materials research. A challenge often encountered in imaging techniques is the need to quantify the changes between two states of the object under inspection. This includes e.g. the deformation induced to a sample by external forces or the misalignment of a specimen between two consecutive CT scans. The estimated deformation can then be used to study mechanical properties like strain [1], which is important e.g. in clinical applications [2, 3] or in experimental mechanics [4, 5]. Digital motion estimation is a key tool to find and determine deformations from digital images as produced by CT and is still a topic with a lot research devoted to. Due to the vast amount of literature concerned with motion estimation, we refer to two reviews, see [6, 7].

Conventional approaches for CT imaging use the reconstructed image data to perform the deformation estimation. In this work, we develop an approach to estimate the affine deformation of a sample directly from the tomographic projections. Working directly with the projection data has three main advantages. First, the standard reconstruction techniques, e.g. filtered backprojection [8], are computationally expensive and have a scaling behavior of  $\mathcal{O}(M^{d+1})$ , where  $M$  is the linear number of voxels in the reconstructed  $d$ -dimensional image volume. As modern CT systems obtain detector resolutions of up to  $2,048 \times 2,048$  pixels, even state-of-the-art hardware becomes as bottleneck in the reconstruction process. Second, in order to obtain reconstructions with good image quality, the number of projection images should roughly be the same as the linear number of voxels in the reconstructed volume [9]. We will show that our direct approach needs considerably less projections, resulting

in reduced scanning time and lowered radiation dose. Third, the standard filtered backprojection is prone to reconstruction artifacts, since artifacts which are localized in the projections are smeared out over the reconstructed volume, resulting in streaks, see e.g. [10]. These streaks are no longer localized and can hence seriously disturb any further image processing method, e.g. motion estimation.

Approaches for estimating deformations directly in the projections have recently received a lot of attention. In [11–13], a projection-based registration of two-dimensional datasets using rigid body transformation is discussed. In [14], these ideas are extended to three-dimensional datasets, allowing (non-uniform) scaling, translation and rotation as degrees of freedom. Due to the use of a Fourier phase matching method, this approach is very fast, but has the disadvantage that the maximum rotation angle around the  $x$  and  $y$  axis must be less than  $10^\circ$ . A modification of this approach was recently applied to problems in the field of nondestructive testing [15]. Another approach for parallel, fan and cone beam geometry is discussed in [16], but again only translation and rotation are allowed. Also, some authors use the Radon transform as a tool to determine affine transformations of images, see [17–22]. As these approaches assume knowledge of the underlying image, they cannot be directly compared to our situation, but give valuable insight into the mathematics of projection based image registration. In contrast to all these approaches, we develop a method which incorporates all degrees of freedom of an affine transformation, that is, rotation, translation, non-uniform scaling and non-uniform shearing. Furthermore, our approach works with two- and three-dimensional parallel and fan beam geometries. Preliminary results of our efforts (using only simulated two dimensional parallel beam geometry) have already been published in [23].

This paper is organized as follow: In Sect. 2, the Radon transform is introduced as a tool to describe the mathematics behind computed tomography, and the parallel and fan beam scanning geometries are explained. Also, we briefly discuss the simulation of tomographic projections, which is needed for our further arguments. In Sect. 3, the motion estimation approach is presented, the results using simulated and experimental data are shown in Sect. 4. Section 5 concludes the paper with a summary and a short outlook.

## 2 Radon transform and computed tomography

We start by introducing the two dimensional Radon transform. Consider a function  $f(\mathbf{x})$  defined for  $\mathbf{x} \in \mathbb{R}^2$ , then its Radon transform is given as [24]

$$\begin{aligned} \tilde{f}(p, \xi_\theta) &:= \mathcal{R}_\theta[f(\mathbf{x}), p] \\ &:= \iint_{\Omega} f(\mathbf{x}) \delta(p - \langle \xi_\theta, \mathbf{x} \rangle) d\mathbf{x}, \end{aligned} \quad (1)$$

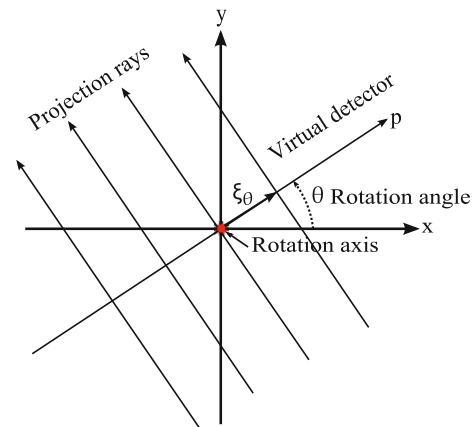


**Fig. 1** Two-dimensional Radon transform.  $p$  is the signed distance from the origin of the coordinate system,  $\theta$  is the rotation angle

where  $\xi_\theta \in \mathbb{S}^1$  is a unit vector,  $\Omega \subseteq \mathbb{R}^2$ ,  $\mathbb{S}^1$  the unit circle and  $\xi_\theta$  is given by  $\xi_\theta = (\cos(\theta), \sin(\theta))^T$ , cf. Fig. 1.

### 2.1 Computed tomography

In X-ray CT, the investigated sample is placed between an X-ray source and a detector device, which measures the intensity of the transmitted X-rays  $I_{tr}$ . By rotating the object in small steps  $\Delta\theta$ , an absorption contrast image is generated for every angle  $\theta$ . For a monochromatic beam with incident intensity  $I_0$ , the normalized measured intensity  $\frac{I_{tr}}{I_0}$  is

$$\frac{I_{tr}}{I_0} = \exp\left(-\int_L f(s) ds\right) \quad (2)$$

where  $L$  is a projection line through the object and  $f(s)$  the material dependent attenuation coefficient.

### 2.2 Scanning geometries

We introduce two types of scanning geometries, namely the parallel beam and the fan beam geometry.

#### 2.2.1 Parallel beam geometry

In the two-dimensional case, the parallel beam geometry can be directly written as Radon transform Eq. 1. The variable  $p$  in Eq. 1 describes the detector coordinate and  $\theta$  the projection angle.

#### 2.2.2 Fan beam geometry

In two dimensions, the fan beam geometry is described as

$$F_{\beta,D}[f(\mathbf{x}), s] = \iint_{\Omega} f(\mathbf{x}) \delta(s \times \cos(\gamma) - \langle \xi_{\beta-\gamma}, \mathbf{x} \rangle) d\mathbf{x}, \quad (3)$$

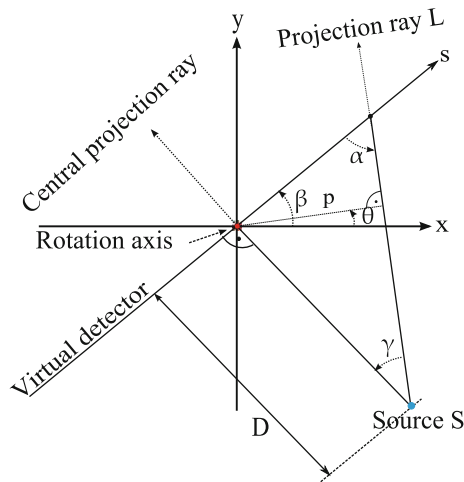


**Fig. 2** Fan beam geometry. To avoid confusion with the parallel beam geometry, we denote the virtual detector coordinate with  $s$  and the rotation angle with  $\beta$ .  $\gamma$  is the angle between the central projection ray and the projection ray  $L$ , while  $D$  is the distance between the detector and the source. Also shown are  $p$  and  $\theta$  if the ray  $L$  would come from the parallel beam geometry

with  $D$  the source to origin distance,  $\beta$  the projection angle,  $\xi_{\beta-\gamma} = \begin{pmatrix} \cos(\beta-\gamma) \\ \sin(\beta-\gamma) \end{pmatrix}$  and  $\gamma$  the angle between the central ray ( $s = 0$ ) and the current ray. Here we use the symbol  $s$  instead of  $p$  for the detector coordinate, in order to avoid confusion with the parallel beam transform. Note that the dependency of  $\gamma$  from  $s$  and  $D$  is hidden, i.e.  $\gamma = \gamma(s, D) = \cos^{-1}(\frac{D}{\sqrt{D^2+s^2}})$ . The fan beam geometry is shown in Fig. 2. Using interpolation, it is possible to resort the fan beam geometry to the parallel beam geometry, with

$$\left. \begin{aligned} \gamma + \alpha &= \frac{\pi}{2} \\ \beta - \theta + \alpha &= \frac{\pi}{2} \end{aligned} \right\} \Rightarrow \beta - \gamma = \theta \quad (4)$$

and

$$\left. \begin{aligned} \cos(\gamma) &= \frac{D}{\sqrt{D^2+s^2}} \\ p &= s \cos(\gamma) \end{aligned} \right\} \Rightarrow p = \frac{sD}{\sqrt{D^2+s^2}}. \quad (5)$$

It is also possible to formulate the three-dimensional (slice by slice) fan beam equation, but we will not use it for our further arguments, hence it is not discussed here.

### 2.3 Simulation of tomographic projections

Expression Eq. 2 is used as a starting point for our simulation of the tomographic projections. The integral in Eq. 2 is substituted by a discrete sum and accounts for typical CCD photon counting noise by replacing the deterministic values of  $I_{tr}$  by Poisson distributed values, i.e.

$$\tilde{I}_{tr} \sim \text{Poisson} \left( I_0 \exp \left( - \int_L f(s) ds \right) \right). \quad (6)$$

It is well-known that the signal-to-noise ratio of a CCD device is proportional to the square root of the detected photons, hence scanning an object with a higher  $I_0$  will result in a better image quality. We can therefore use  $I_0$  as a steering parameter to control the quality of the obtained projections. For a given image  $f(\mathbf{x})$  and a given set of projection angles  $\Theta$ , the simulated sinogram therefore consists of  $\tilde{I}_{tr}$ , computed at the angles  $\theta \in \Theta$ .

## 3 Methods

### 3.1 Affine transformations and the Radon transform

Affine transformations consist of rotation, translation, scaling and shearing. Using matrices, affine transformations can be constructed in two dimensions with

$$\mathbf{T}_a(\mathbf{x}) = \underline{A}_a \mathbf{x} + \mathbf{u} \quad (7)$$

where

$$\underline{A}_a = \underline{A}_{\text{rot}} \cdot \underline{A}_{\text{scale}} \cdot \underline{A}_{\text{shear}} \quad (8)$$

and

$$\mathbf{u} = \begin{pmatrix} u_x \\ u_y \end{pmatrix}, \quad \underline{A}_{\text{rot}} = \begin{pmatrix} \cos(\varphi) & -\sin(\varphi) \\ \sin(\varphi) & \cos(\varphi) \end{pmatrix}, \quad (9)$$

$$\underline{A}_{\text{scale}} = \begin{pmatrix} sx & 0 \\ 0 & sy \end{pmatrix}, \quad \underline{A}_{\text{shear}} = \begin{pmatrix} 1 & shx \\ shy & 1 \end{pmatrix}.$$

Similar constructions hold for the three dimensional case, see e.g. [25]. Inserting the transformation Eq. 7 into the Radon transform Eq. 1 yields

$$\begin{aligned} \mathcal{R}_\theta [f(\underline{A}_a \mathbf{x} + \mathbf{u}), p] \\ = \left\| \det(\underline{A}_a^{-1}) \right\| \check{f} \left( p + \langle \underline{A}_a^{-\top} \xi_\theta, \mathbf{u} \rangle, \underline{A}_a^{-\top} \xi_\theta \right). \end{aligned} \quad (10)$$

As  $\underline{A}_a^{-\top} \xi_\theta$  is generally not a unit vector anymore, we normalize the arguments of Eq. 10, resulting in

$$\begin{aligned} \mathcal{R}_\theta [f(\underline{A}_a \mathbf{x} + \mathbf{u}), p] \\ = \frac{\left\| \det(\underline{A}_a^{-1}) \right\|}{\left\| \underline{A}_a^{-\top} \xi_\theta \right\|} \check{f} \left( \frac{p + \langle \underline{A}_a^{-\top} \xi_\theta, \mathbf{u} \rangle}{\left\| \underline{A}_a^{-\top} \xi_\theta \right\|}, \frac{\underline{A}_a^{-\top} \xi_\theta}{\left\| \underline{A}_a^{-\top} \xi_\theta \right\|} \right), \end{aligned} \quad (11)$$

where we have used the identity  $\delta(ax) = \frac{1}{|a|} \delta(x) \forall x \in \mathbb{R}$  and  $\forall a \in \mathbb{R} \setminus 0$ . We therefore notice that any affine mapping acts on the projection data in three different ways, namely by translation with respect to the  $p$  axis ( $p \mapsto p + \langle \underline{A}_a^{-\top} \xi_\theta, \mathbf{u} \rangle$ ), scaling of the  $p$ -axis (division by  $\left\| \underline{A}_a^{-\top} \xi_\theta \right\|$ )

and rotating  $\xi_\theta (\xi_\theta \mapsto \frac{\underline{A}_a^{-\top} \xi_\theta}{\|\underline{A}_a^{-\top} \xi_\theta\|})$ . The rotation angle is given by

$$\varphi = \arccos \left( \frac{\langle \xi_\theta, \underline{A}_a^{-\top} \xi_\theta \rangle}{\|\underline{A}_a^{-\top} \xi_\theta\|} \right). \quad (12)$$

We will later show that the factor  $\frac{\|\det(\underline{A}_a^{-1})\|}{\|\underline{A}_a^{-\top} \xi_\theta\|}$  has no influence on our estimation approach and can therefore be neglected.

### 3.2 Parameter-estimation procedure

We introduce the notation  $\check{f}(\check{\mathbf{T}}_a(p), \check{\mathbf{T}}_a(\xi_\theta))$  to express the action of the affine transformation  $\mathbf{T}_a$  on the Radon transform  $\check{f}(p, \xi_\theta)$ . The inverse problem is formulated by

**Definition 1** Let  $\mathbf{T}_a$  be a regular affine mapping and  $f_{\text{def}}(\mathbf{x}) = f_{\text{ref}}(\mathbf{T}_a(\mathbf{x}))$  two unknown images with known Radon transforms  $\mathcal{R}_\theta[f_{\text{ref}}(\mathbf{x})]$  and  $\mathcal{R}_\theta[f_{\text{def}}(\mathbf{x})]$ , respectively. For the target function

$$\mathcal{E}(\mathbf{T}_{\text{est}}) = \frac{1}{2} \sum_{\theta \in \Theta} (\psi(\mathbf{T}_{\text{est}}, \theta))^2, \quad (13)$$

find the affine mapping  $\mathbf{T}_{\text{est}}^*$ , such that

$$\mathbf{T}_{\text{est}}^* = \arg \min_{\mathbf{T}_{\text{est}} \in \mathcal{A}} \mathcal{E}(\mathbf{T}_{\text{est}}). \quad (14)$$

Here,

$$\psi(\mathbf{T}_{\text{est}}, \theta) = \mathcal{S} \left( \check{f}_{\text{ref}}(\check{\mathbf{T}}_{\text{est}}(p), \check{\mathbf{T}}_{\text{est}}(\xi_\theta)), \check{f}_{\text{def}}(p, \xi_\theta) \right) \quad (15)$$

is a similarity measure,  $\Theta$  is the set of all projection angles and  $\mathcal{A}$  is the set of affine mappings.

As similarity measure  $\mathcal{S}(\cdot, \cdot)$ , we choose normalized cross correlation [26], hence

$$\mathcal{S}(\cdot, \cdot) = 1 - \text{NCC}(\cdot, \cdot), \quad (16)$$

with

$$\begin{aligned} \text{NCC}(I_1, I_2) \\ = 1 - \frac{\sum_{\mathbf{x}} (I_1(\mathbf{x}) - \bar{I}_1)(I_2(\mathbf{x}) - \bar{I}_2)}{(\sum_{\mathbf{x}} (I_1(\mathbf{x}) - \bar{I}_1)^2 \sum_{\mathbf{x}} (I_2(\mathbf{x}) - \bar{I}_2)^2)^{\frac{1}{2}}}. \end{aligned} \quad (17)$$

Here,  $\bar{I}_1$  and  $\bar{I}_2$  are the arithmetic means of  $I_1$  and  $I_2$ , respectively. An important property of the normalized cross correlation Eq. 17 is its invariance under linear transformations, i.e.  $\text{NCC}(I_1, aI_2 + b) = \text{NCC}(I_1, I_2)$  for  $a, b \in \mathbb{R}, a \neq 0$ .

This allows us to ignore the constant factor  $\frac{\|\det(\underline{A}_a^{-1})\|}{\|\underline{A}_a^{-\top} \xi_\theta\|}$  in Eq. 11, which simplifies the optimization process.

### 3.3 Optimization algorithm

In order to solve the minimization problem Eq. 13, a trust-region based optimizer is used, see e.g. [27]. Starting with an initial estimate  $\mathbf{t}_{\text{est}}^0$  (understand the vector  $\mathbf{t}_{\text{est}}$  as the parameters of the transformation  $\mathbf{T}_{\text{est}}$ ), the algorithm iteratively (iteration index  $k$ ) computes better approximations on the subspace, the trust region, around the current position, i.e.

$$\mathbf{t}_{\text{est}}^{k+1} = \mathbf{t}_{\text{est}}^k + \Delta \mathbf{t}, \quad (18)$$

with  $\Delta \mathbf{t}$  determined by

$$\min_{\Delta \mathbf{t}} : \frac{1}{2} \Delta \mathbf{t}^\top \underline{H}_\psi \Delta \mathbf{t} + \Delta \mathbf{t}^\top \underline{J}_\psi \quad \text{subject to} \quad \|\underline{D} \Delta \mathbf{t}\| \leq \rho^k, \quad (19)$$

where  $\underline{H}_\psi$  is the Hessian matrix,  $\underline{J}_\psi$  is the Jacobian matrix of  $\psi$  with respect to  $\mathbf{t}$ ,  $\underline{D}$  is a diagonal scaling matrix and  $\rho^k$  a positive scalar. The solution of Eq. 19 can approximately be found by computing a Gauss–Newton direction, given as solution of the least squares problem

$$\underline{J}_\psi \Delta \mathbf{t} = -\Delta \psi, \quad (20)$$

where  $\Delta \psi$  is the vector of residuals of the target function, i.e.

$$\Delta \psi = \left( \psi(\mathbf{T}_{\text{est}}^k, \theta_1), \psi(\mathbf{T}_{\text{est}}^k, \theta_2), \dots \right)^\top. \quad (21)$$

Finally,  $\Delta \mathbf{t}$  is accepted if

$$\mathcal{E}(\mathbf{t}_{\text{est}}^k + \Delta \mathbf{t}) < \mathcal{E}(\mathbf{t}_{\text{est}}^k), \quad (22)$$

and  $\rho^{k+1}$  is increased. If  $\Delta \mathbf{t}$  is rejected,  $\rho^{k+1}$  is decreased and the step is repeated. The iteration is terminated if either the target function is smaller than a user defined threshold  $\mathcal{E}_{\text{tol}}$ , or the iteration stagnates, i.e.  $\|\mathbf{t}_{\text{est}}^{k+1} - \mathbf{t}_{\text{est}}^k\| < \epsilon_{\text{tol}}$ , where  $\epsilon_{\text{tol}}$  is again a user defined tolerance. The search of the Gauss–Newton direction needs no second derivatives (i.e. no Hessian matrix), which reduces the memory usage, as only the projection data and the Jacobian must be available. To compute the Jacobian matrix  $\underline{J}_\psi$ , we use three point centered finite differences to approximate derivatives. The optimization procedure does therefore directly search for the optimal parameters of  $\mathbf{T}_{\text{est}}$ , i.e. the rotation, scaling, shearing and translation composition in Eqs. 8 and 9 is not used.

#### 3.3.1 Spline interpolation

The evaluation of the target function Eq. 13 for the current estimate  $\mathbf{T}_{\text{est}}$  may need projection data at coordinates  $(p, \theta)$  which are not available due to the limited detector resolution and the finite number of projection angles. A cubic spline [28] is used to interpolate the projections at arbitrary coordinates. Using cubic splines as interpolation method has the advantage that the resulting function is smooth up to order

two. Also, evaluating a given spline interpolation is fast, as the B-spline basis functions have only small support.

### 3.3.2 Multiresolution extension

From the definition of the affine transformation  $\mathbf{T}_a$ , it can be seen that the absolute values of the translational part (i.e. the vector  $\mathbf{u}$ ) are typically larger than the components of the linear part (i.e. the matrix  $\mathbf{A}_a$ ). It is reasonable to assume that  $-20 \leq u_x, u_y \leq 20$ , but typically for the components  $a_{ij} \in \mathbf{A}_a$  it holds  $-1.5 \leq a_{ij} \leq 1.5$ . This does also mean that a given increment  $\Delta t$  in Eq. 18 has more influence on  $\mathbf{A}_a$  than on  $\mathbf{u}$ . Although this effect should be somewhat compensated by the smaller derivatives (with respect to  $u_x$  and  $u_y$ ) of the target function Eq. 13, we prefer to implement a multiscale [29] extension for the translational part. As translations do only act on the  $p$  coordinate of the Radon transform, the multiscale representation is obtained by downsampling  $\mathcal{R}_\theta[f(\mathbf{x}), p]$  with respect to  $p$ . We denote the Radon transform at level  $l$  by  $\mathcal{R}_\theta[f(\mathbf{x}), p^l]$ , with the convention that  $\mathcal{R}_\theta[f(\mathbf{x}), p^0] := \mathcal{R}_\theta[f(\mathbf{x}), p]$ . In every downsample step  $l \mapsto l+1$ , the size of the projection data in  $p$ -direction is reduced by a factor of two. Most importantly, the magnitude of a translation  $p' = p + \Delta u$  is also reduced by a factor of two, i.e.  $\Delta u^l = \frac{1}{2} \Delta u^0$ . The modified optimization procedure then reads: Iterate for  $l = L, L-1, \dots, 0$

1. Compute spline interpolation(s) of  $\mathcal{R}_\theta[f_{\text{ref, def}}(\mathbf{x}), p^l]$ .
2. Find best affine parameters on the level  $l$ , denoted by  $\mathbf{t}_{\text{est}, l}^*$ .
3. Upscale translational part of  $\mathbf{t}_{\text{est}, l}^*$  by multiplication with a factor of 2.
4. Use the upscaled version of  $\mathbf{t}_{\text{est}, l}^*$  as initial estimate  $\mathbf{t}_{\text{est}, l-1}^0$  for the next iteration level, go back to 1.

To avoid aliasing due to undersampling, we apply Gaussian smoothing prior to the downsampling, using a filter length of 7 pixels and a standard deviation of  $\sigma = 1$ .

### 3.4 Three-dimensional parallel beam

The definition of the Radon transform Eq. 1 can be extended to three dimensions by choosing  $\mathbf{x} \in \mathbb{R}^3$  and  $\xi_{\theta_{1,2}} \in \mathbb{S}^2$ . A possible (but not unique) choice for  $\xi_{\theta_{1,2}}$  is  $\xi_{\theta_{1,2}} = (\cos(\theta_1) \sin(\theta_2), \sin(\theta_1) \sin(\theta_2), \cos(\theta_2))^T$ , see also Fig. 3. Similar to Eq. 1, we write

$$\begin{aligned} \check{f}(p, \xi_{\theta_{1,2}}) &:= \mathcal{R}_{\theta_{1,2}}[f(\mathbf{x}), p] \\ &:= \iiint_{\Omega} f(\mathbf{x}) \delta(p - \langle \xi_{\theta_{1,2}}, \mathbf{x} \rangle) d\mathbf{x}. \end{aligned} \quad (23)$$

Note that in the three-dimensional case, the Radon transform integrates over planes, whereas the integration is over

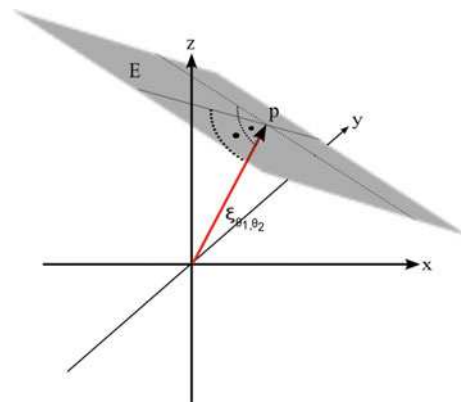


**Fig. 3** Three-dimensional Radon transform. Integration area is the plane  $E$  with signed distance  $p$  from the origin of the coordinate system. The vector  $\xi_{\theta_{1,2}}$  does depend on two angles  $\theta_{1,2}$

lines in the two-dimensional case. We may understand the three-dimensional parallel beam transform as a slice by slice scanning of a three-dimensional sample, each slice is then described by a two-dimensional Radon transform. Formally, this can be described as

$$\begin{aligned} \check{f}(p, t, \xi_\theta, \mathbf{e}_3) &= \iiint_{\Omega} f(\mathbf{x}) \delta(p - \langle \xi_\theta, \mathbf{x} \rangle) \delta(t - \langle \mathbf{e}_3, \mathbf{x} \rangle) d\mathbf{x}, \end{aligned} \quad (24)$$

where  $\xi_\theta = (\cos \theta, \sin \theta, 0)^T$  and  $\mathbf{e}_3 = (0, 0, 1)^T$ . Thus, the integration line is described by an intersection of 2 planes through the volume  $f(\mathbf{x})$ ,  $p$  and  $t$  are the horizontal and vertical detector coordinates, respectively. As a consequence, Eq. 24 cannot be equal to the three dimensional version of the Radon transform Eq. 23. However, we can compute a sample of the three-dimensional Radon transform by applying a two-dimensional Radon transform to the projection data obtained from Eq. 24. Consider for this

$$\underbrace{\iint_{\Omega_D} \check{f}(p, t, \xi_\theta, \mathbf{e}_3) \delta(p_2 - \langle \xi_{\theta_2}, (t, p)^T \rangle) dp dt}_{\substack{\text{3d para. beam transf.} \\ \text{2d Radon transform of the projections over } p \text{ and } t}} \quad (25)$$

with  $\xi_{\theta_2} = (\cos(\theta_2), \sin(\theta_2))^T$ ,  $p_2$  the signed distance of the line  $\langle \xi_{\theta_2}, (t, p)^T \rangle = 0$  to the origin ( $p = 0, t = 0$ ) and  $\Omega_D$  the detector area. A necessary condition for the non-triviality of the integral Eq. 25 is

$$t - \langle \mathbf{e}_3, \mathbf{x} \rangle = 0 \Rightarrow t = z \quad (26)$$

and

$$p_2 - t \cos(\theta_2) - p \sin(\theta_2) = 0. \quad (27)$$



Hence,

$$p = \frac{p_2}{\sin(\theta_2)} - z \frac{\cos(\theta_2)}{\sin(\theta_2)}. \quad (28)$$

Inserting Eqs. 26 and 27 into Eq. 25 then yields

$$\iiint_{\Omega} f(\mathbf{x}) \delta \left( \frac{p_2}{\sin(\theta_2)} - z \frac{\cos(\theta_2)}{\sin(\theta_2)} - \langle \tilde{\xi}_\theta, \mathbf{x} \rangle \right) d\mathbf{x} \quad (29)$$

$$= \iiint_{\Omega} f(\mathbf{x}) \delta(p_2 - \langle \xi_{\theta_{1,2}}, \mathbf{x} \rangle) d\mathbf{x} \quad (30)$$

$$= \mathcal{R}_{\theta_{1,2}}[f(\mathbf{x}), p_2], \quad (31)$$

which is exactly the Radon transform in  $\mathbb{R}^3$ . Therefore, computation of the three dimensional Radon transform is possible if three dimensional parallel beam projection data is available. However, the computation of the Radon transform has similar computational complexity as the standard image reconstruction process, hence this approach makes only sense if less projections must be computed. For the sake of clarity, we rewrite the target function Eq. 13 as

$$\mathcal{E}(\mathbf{T}_{\text{est}}) = \frac{1}{2} \sum_{\theta_1, \theta_2 \in \Theta_1 \times \Theta_2} (\psi(\mathbf{T}_{\text{est}}, \theta_1, \theta_2))^2, \quad (32)$$

where  $\Theta_1$  is the set of projection angles for the three dimensional parallel beam transform and  $\Theta_2$  is the set of projection angles of the two dimensional Radon transform. We may then apply the same estimation/optimization procedure as in Sects. 3.2 and 3.3 to determine the parameters of the three-dimensional affine transformation.

### 3.4.1 Sparse evaluation of the target function

To speed up the computation in the main iteration loop, it is possible to use only a limited number of angle pairs  $(\theta_1, \theta_2)$  for the computation of the target function (Eq. 32). As every profile  $\mathcal{R}_{\theta_{1,2}}[f(\mathbf{x}), \cdot]$  of the Radon transform contains projection data from the full sample in image space, this is not equivalent to a restriction of the image volume to a subvolume. However, in order to keep the spline interpolation reasonably accurate, all profiles of the Radon transform must be used for the computation of the interpolation spline. Hence, only the evaluation of the target function is accelerated, but as this evaluation must be done in every optimization iteration loop, it is computationally far more expensive than the spline interpolation. Let  $k$  be the fraction of profiles used for the evaluation of the target function (e.g.  $k = 0.05$  corresponds to 5% of all profiles), then the expected speedup is  $\approx \frac{1}{k}$ .

## 3.5 Application to the fan beam geometry

We can directly apply the transformation from Eq. 11 to the image data  $f(\mathbf{x})$ , resulting in

$$F_{\beta, D}[f(\underline{A}_a \mathbf{x} + \mathbf{u}), s] = \frac{\|\det(\underline{A}_a^{-1})\|}{\|\underline{A}_\xi\|} \times \iint_{\Omega} f(\mathbf{y}) \delta \left( \frac{s \cdot \cos(\gamma) + \langle \underline{A}_\xi, \mathbf{u} \rangle}{\|\underline{A}_\xi\|} - \left\langle \frac{\underline{A}_\xi}{\|\underline{A}_\xi\|}, \mathbf{y} \right\rangle \right) d\mathbf{y}, \quad (33)$$

where we have set  $\underline{A}_\xi := \underline{A}_a^{-\top} \xi_{\beta-\gamma}$ . Although Eq. 33 is conceptually equivalent to Eq. 11, there are three major drawbacks for its practical use. First, the factor  $\frac{\|\det(\underline{A}_a^{-1})\|}{\|\underline{A}_a^{-\top} \xi_{\beta-\gamma}\|}$  does not only depend on the transformation  $\underline{A}_a$  and the rotation angle  $\beta$ , but also on the ray angle  $\gamma$  (and hence on  $s$  and  $D$ ). While the dependency on  $D$  is not an issue (as the source-origin distance is constant during the scan), the dependency on  $s$  means that  $\frac{\|\det(\underline{A}_a^{-1})\|}{\|\underline{A}_a^{-\top} \xi_{\beta-\gamma}\|}$  cannot be neglected in the computation of the target function Eq. 13, as the normalized cross correlation similarity measure (Eq. 17) is not invariant under transformations of  $s$ . Second, the transformed vector  $\frac{\underline{A}_a^{-1} \xi_{\beta-\gamma}}{\|\underline{A}_a^{-\top} \xi_{\beta-\gamma}\|}$  must be computed for every  $\beta$  and for every  $\gamma$ . As this computation is performed in every iteration step, this increases the computational load. The third problem is a bit more subtle. Assume, without loss of generality, that  $\underline{A}_a = \mathbb{E}$ ,  $\mathbf{u} = (u_x, 0)^\top$  and  $\beta = \gamma = 0^\circ$ , hence we are looking at the central projection ray, which hits the detector at  $s = 0$ . Looking at the deformed geometry, the corresponding detector coordinate according to Eq. 33 is  $s' = 0 + \langle \xi_{\beta-\gamma}, \mathbf{u} \rangle = u_x$ , which equals a scanning geometry translated by  $u_x$  parallel to the detector. However, for such a geometry, no projection data is available, as the ray with  $s' = u_x$  is not the central projection ray (i.e.  $\gamma \neq 0^\circ$ ). However, an equivalent ray (which must be parallel to the original ray) can be found by choosing  $\beta'$  and  $\gamma'$  of the new ray appropriately. The mapping  $\beta \mapsto \beta'$  and  $\gamma \mapsto \gamma'$  is exactly the transformation from fan beam to parallel beam, and this transformation must be done for every detector coordinate in every iteration of the optimization procedure, see also Fig. 4. Due to these drawbacks, it is preferable to convert fan beam data to parallel beam data prior to the motion estimation. This can be done simultaneously to the projection acquisition and does not increase the computational burden significantly. After the fan beam to parallel beam mapping, the parallel beam estimation procedure can be used to determine the affine transformation. For the 3d fan beam case, the same approach is advisable, such that the procedures from Sect. 3.4 can be used.

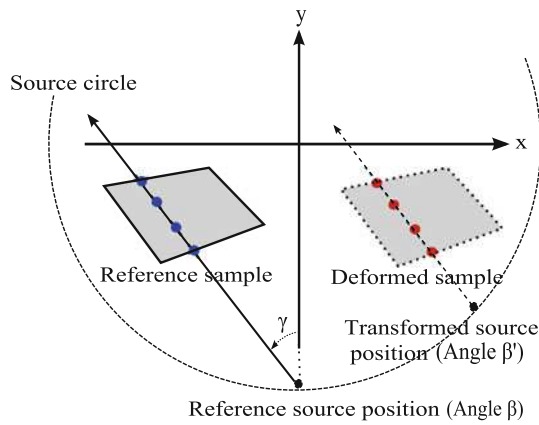


**Fig. 4** Fan beam geometry and deformation. We are considering the ray which passes through the four dots in the reference sample. In the deformed (here, deformed mean translated parallel to the  $x$  axis) sample, the ray which passes through the equivalent four dots does not originate from the same source position and is parallel to the original ray. Hence the transformation is the fan beam to parallel beam mapping

### 3.6 Computational complexity

We investigate the computational complexity of the three major parts of the two dimensional estimation approach:

- Spline interpolation;
- Evaluation of the target function;
- Solution of the least squares problem in the trust region optimizer;

Due to the small support of the B-spline basis functions, the complexity of the spline interpolation is linear with respect to the number of interpolation sites. Let  $\|\Theta\|$  be the number of projection angles and  $N_p$  the number of detector coordinates, then the B-spline interpolation (as well as the evaluation) has a complexity of

$$\mathcal{C}_{\text{spline}} = \mathcal{O}(\|\Theta\| \cdot N_p). \quad (34)$$

The evaluation of the of the target function is dominated by the computation of the normalized cross correlation, i.e.

$$\mathcal{C}_{\text{tf}} = \mathcal{O}(\|\Theta\| \cdot N_p). \quad (35)$$

Solving the least squares problem involves the computation of the Jacobian, using  $\mathcal{O}(\|\Theta\| \cdot \text{dof})$  operations, where  $\text{dof}$  is the number of degrees of freedom, i.e. 6 for the two dimensional affine case. The resulting linear system can be solved in  $\mathcal{O}(\|\Theta\| \cdot \text{dof}^2)$  steps, e.g. by applying a QR factorization. Hence, one step of the trust region optimizer costs

$$\mathcal{C}_{\text{opt}} = \mathcal{O}(\|\Theta\| \cdot (\text{dof} + \text{dof}^2)). \quad (36)$$

Accounting for the fact that the computation of the target function and the solution of the linear system must be done in

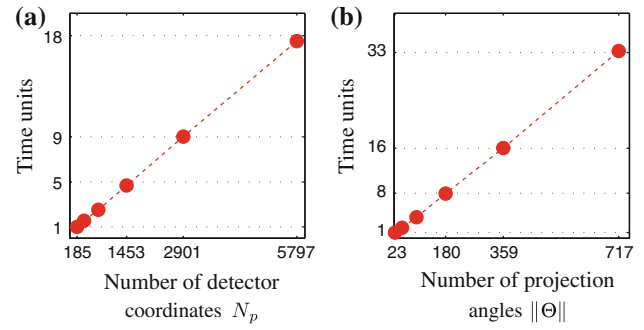


**Fig. 5** Complexity of the deformation estimation. Time units needed for 10 iterations of the optimization algorithm versus the number of detector coordinates  $N_p$  (a). Time units needed for 10 iterations of the optimization algorithm versus the number of projection angles  $\|\Theta\|$  used (b)

every iteration step of the optimization procedure, we finally deduce that the overall complexity is given by

$$\mathcal{C}_{2d} = \mathcal{O}(N_{it} \cdot \|\Theta\| \cdot (2 \cdot N_p + \text{dof} + \text{dof}^2)), \quad (37)$$

where  $N_{it}$  is the number of iterations of the optimization procedure. As usually  $N_p \gg \text{dof} + \text{dof}^2$ , we can approximate Eq. 37 by

$$\mathcal{C}_{2d} \approx \mathcal{O}(2 \cdot N_{it} \cdot \|\Theta\| \cdot N_p). \quad (38)$$

If the additional effort for the multiscale approach is also taken into account, we get

$$\mathcal{C}_{2d, \text{multiscale}} \approx \mathcal{O}(4 \cdot N_{it} \cdot \|\Theta\| \cdot N_p), \quad (39)$$

as the number of detector coordinates at level  $l$  is given by  $\frac{1}{2^l} \cdot N_p$  and  $\lim_{L \rightarrow \infty} \sum_{l=0}^L \frac{1}{2^l} = 2$ , and this number is not dependant on  $L$ . Comparing Eq. 39 to the  $\mathcal{O}(M^{d+1})$  complexity of standard reconstruction algorithms, we conclude (using  $d = 2$  and  $M \approx N_p$ ) that our approach has roughly the same asymptotical complexity. However, our approach already includes the computational costs for the motion estimation and enables us to choose  $\|\Theta\| < M$  and  $N_{it} < M$ , hence some advantages with respect to the computational complexity can be expected.

Finally, we mention that similar arguments also hold for the three dimensional case. An experimental verification of the arguments above is given in Fig. 5, where the linear scaling of the complexity is verified w.r.t.  $N_p$  and  $\|\Theta\|$ .

## 4 Results

In this section, we present the results for our estimation approach, using simulated and experimental data.

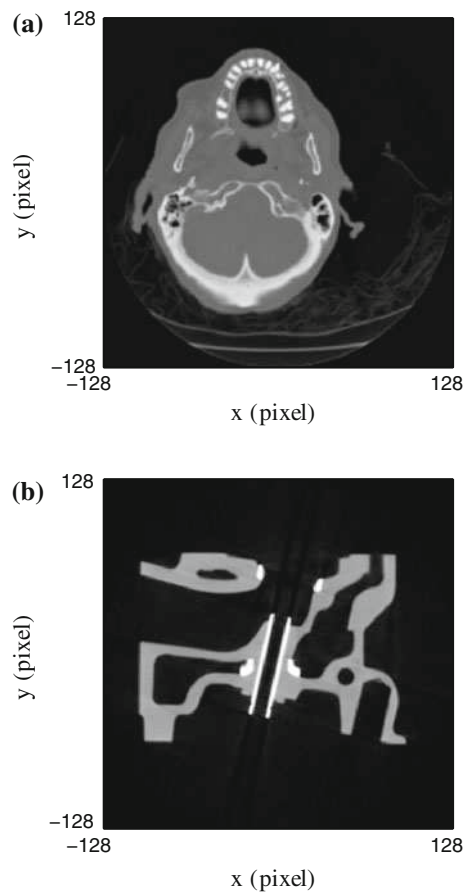


**Fig. 6** Head dataset (a). Engine dataset (b)

#### 4.1 Test data

##### 4.1.1 Two-dimensional data

As test images for the two-dimensional case, we use two different datasets:

**Head:** A cross section of a human head Fig. 6a,  $256 \times 256$  pixels, obtained from <http://www9.informatik.uni-erlangen.de/External/vollib/>.

**Engine:** A cross section of a CT scan of an engine block Fig. 6b,  $256 \times 256$  pixels, obtained from <http://www.volvis.org>.

##### 4.1.2 Three-dimensional data

For the three-dimensional tests, we use the following datasets:

**Engine 3d:** CT scan of two cylinders of an engine block Fig. 7a,  $256 \times 256 \times 128$  voxels, obtained from <http://www.volvis.org>.

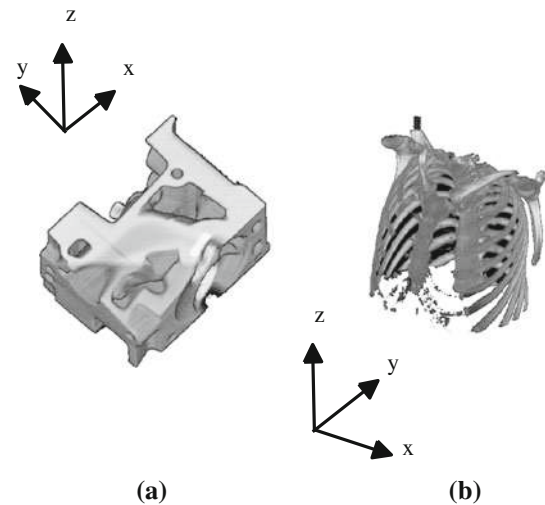


**Fig. 7** Engine 3d dataset (a). Chest dataset (b)

**Chest:** A CT scan of a human chest Fig. 7b,  $384 \times 384 \times 240$  voxels, obtained from <http://www9.informatik.uni-erlangen.de/External/vollib/>.

##### 4.1.3 Experimental data

For our experiments, we use two different test objects. The first is a small beech wood sample, cylindrically shaped with a diameter of roughly 1 mm and a length of roughly 10 mm. The sample is glued to a metallic pin (diameter 3.15 mm) which acts as sample holder. The second sample is a similar cylindrical piece of wood, but the wood type is Scots pine and the wood has been dried at  $140^\circ\text{C}$  prior to the use as a test object. To induce the deformation, both samples are placed in water for several hours (7 and 12 h for the beech and the pine, respectively). The heat treatment of the pine sample is expected to influence the water uptake behavior, but we will not interpret our deformation results in the context of the structural properties of wood. The reader interested in such results is referred to e.g. [30–32]. The measurements are performed at the TOMCAT beamline [33,34] at the Swiss Light Source (SLS), Paul Scherrer Institute, Villigen, Switzerland. Both samples are scanned before and after the water treatment (i.e. the dry and the wet state, respectively), to obtain the reference and the deformed sample, respectively. The data is acquired using synchrotron radiation with an energy of 9.4 keV. After conversion to visible light by a YAG:Ce (yttrium aluminium garnet doped with cerium) scintillator, an objective with 10x magnification is used. The detector resolution is  $2,048 \times 901$  pixel, corresponding to a field of view of  $1.43 \times 0.63$  mm and a pixel size of  $0.7 \times 0.7 \mu\text{m}$ . A total of 1,501 projections in the angular interval  $45^\circ - 225^\circ$  are taken. Exposure time is 480 ms for each projection, resulting in a total scan time of



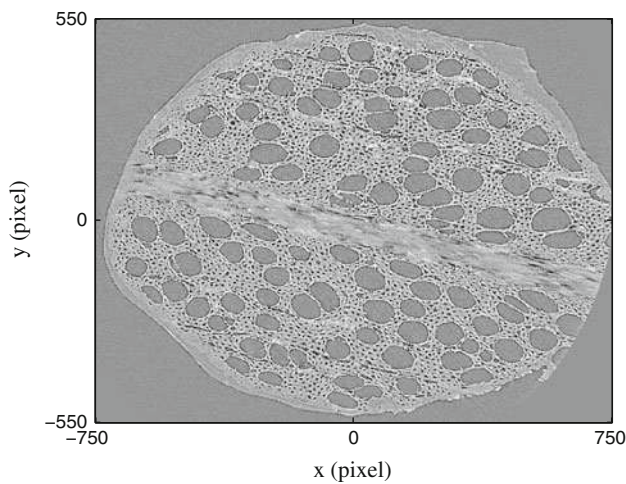


**Fig. 8** “Beech1” dataset (dry state)

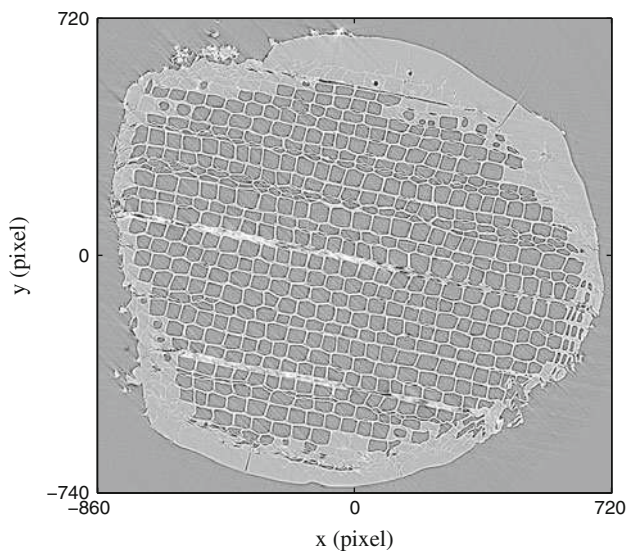


**Fig. 9** “Pine” dataset (wet state). Note the completely different wood structure compared to the beech datasets

roughly 12 min. For the  $2d$  estimation, we extract two  $XY$  planes ( $2,048 \times 2,048$  pixels each) from the reconstructed volumes at two different  $z$  coordinates for the beech sample (“beech1” and “beech2”). The  $z$  coordinates are manually selected such that any deformation in  $z$  direction is approximately compensated. The structural variation in  $z$  direction is much smaller than in  $x$  and  $y$  direction, such that the choice of the  $z$  coordinate is rather uncritical. Similarly, one  $XY$  plane ( $2,048 \times 2,048$  pixels) is extracted from the reconstructed pine wood volume, called “pine” from here on. Finally, a  $3d$  dataset is obtained by cutting a  $2,048 \times 2,048 \times 200$  volume from the full beech volume dataset. Due to the parallel projection geometry, the corresponding sinogram data can easily be located in the sinogram stack and hence be used for our projection based approach. Examples of reconstructed slices (beech and pine) are shown in Figs. 8 and 9.

**Table 1** Test parameters for the simulated data

Parameter	Value(s)
No. of projections $\ \Theta\ $ ( $2d$ )	{180, 90, 45, 23, 12}
No. of projections $\ \Theta_{1,2}\ $ ( $3d$ )	$\ \Theta_1\  = 180, \ \Theta_2\  = 45$
No. of multiscale levels $L$	$L = 3$
Max. number of iterations	50
Fraction of profiles used ( $3d$ only)	$k = 0.05$
No. of incidents photons $I_0$	{500, 1000, 2000, 3000, 5000}

For the  $2d$  tests, the projection angles are chosen equiangular in  $[0^\circ \dots 180^\circ]$

**Table 2** Affine parameter range

Parameter	Value(s)
Translation (pixel) $t_x, t_y, t_z$	$[-20 \dots 20]$
Scaling $s_x, s_y, s_z$	$[0.9 \dots 1.1]$
Shearing $sh_x, sh_y, sh_z$	$[-0.1 \dots 0.1]$
Rotation angle $\varphi_{x,y,z}$	$[-20^\circ \dots 20^\circ]$

$\varphi_{x,y,z}$  denotes rotation around the  $x$ ,  $y$  and  $z$  axis, respectively. For the  $2d$  simulations, only the  $x$  and  $y$  values in every row are used, and the rotation is always perpendicular to the  $xy$ -plane

## 4.2 Error measures

Let  $f_{\text{ref}}$  be the undeformed image,  $\mathbf{T}_a$  the transformation and  $f_{\text{def}} = f_{\text{ref}}(\mathbf{T}_a(\mathbf{x}))$  the deformed image. We then compute an estimated transformation  $\mathbf{T}_{\text{est}}^*$  using the procedure described in Sect. 3. Once  $\mathbf{T}_{\text{est}}^*$  is estimated for the transformation  $\mathbf{T}_a$ , we are able to calculate an estimated deformation vector field  $\mathbf{v}_{\text{est}}$  at every pixel (or voxel) of the test image and compare it to the reference deformation field  $\mathbf{v}_{\text{ref}}$ . We choose the origin of the coordinate system to be in the center of the image and define the mean relative magnitude error as

$$\overline{\psi}_{\text{mag,rel}} = \frac{1}{N} \sum_{j=1}^N \frac{\|\mathbf{v}_{\text{ref}}(\mathbf{x}_j) - \mathbf{v}_{\text{est}}(\mathbf{x}_j)\|}{\|\mathbf{v}_{\text{ref}}(\mathbf{x}_j)\|}, \quad (40)$$

and the mean angular error as

$$\psi_{\text{ang}} = \frac{1}{N} \sum_{j=1}^N \arccos \left( \frac{\langle \mathbf{v}_{\text{ref}}(\mathbf{x}_j), \mathbf{v}_{\text{est}}(\mathbf{x}_j) \rangle}{\|\mathbf{v}_{\text{ref}}(\mathbf{x}_j)\| \|\mathbf{v}_{\text{est}}(\mathbf{x}_j)\|} \right), \quad (41)$$

where  $N$  is the number of pixel or voxel in the image.

## 4.3 Results from simulated data

We simulate the tomographic projection according to the procedures described in Sect. 2.3. The test parameters are given in Table 1, the range of the deformation parameters in Table 2. For each  $I_0$ , we simulate 25 image pairs (reference and deformed) and evaluate the estimated affine transformations according to the error measures Eqs. 40 and 41. For the

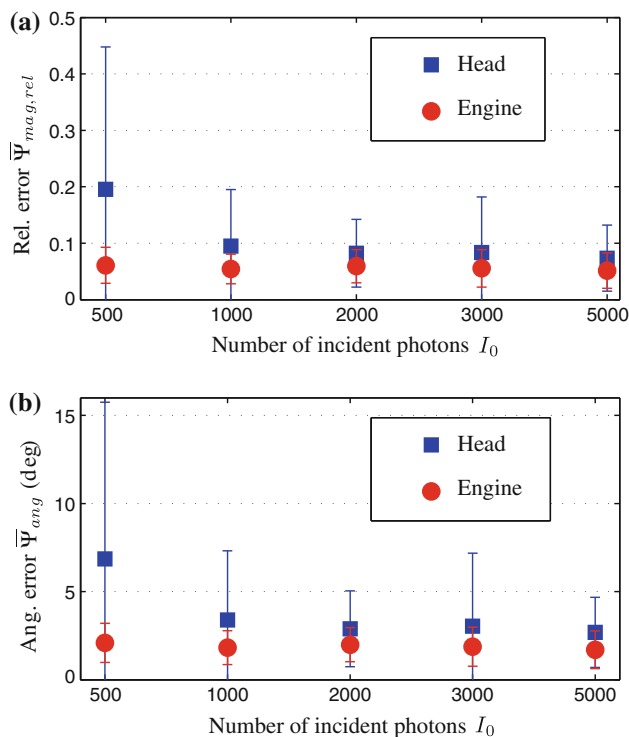


**Fig. 10** Errors for the 2d deformation estimation using the datasets head and engine with different number of incident photons  $I_0$ . Relative error (a). Angular error in degrees (b). In all plots, the standard deviation is also shown

optimization procedure, the identity mapping  $\mathbf{T}_{est}^0(\mathbf{x}) = \mathbf{x}$  was selected as initial estimate. We also tried to enhance the initial estimate by the use of simple method proposed in [35], which is able to recover translation and scaling using a very fast center-of-mass approach. However as our deformation also includes rotation and shearing, the obtained initial estimates did not yield any improvement compared to the identity mapping.

#### 4.3.1 2d datasets

From Fig. 10, we see that both test datasets perform well, with the relative error approximately 10% and the angular error approximately  $5^\circ$  for most test runs. The influence of the number of photons  $I_0$  is only significant for  $I_0 = 500$  for the head dataset, proving the robustness of our estimation technique with respect to the signal to noise ratio of the tomographic projections.

#### 4.3.2 3d datasets

The estimation results for the 3d datasets are shown in Fig. 11. The estimation accuracy for all datasets is independent of the value of  $I_0$  used for testing. The reason for this is clearly the fact that the 2d Radon transform (i.e. the outer

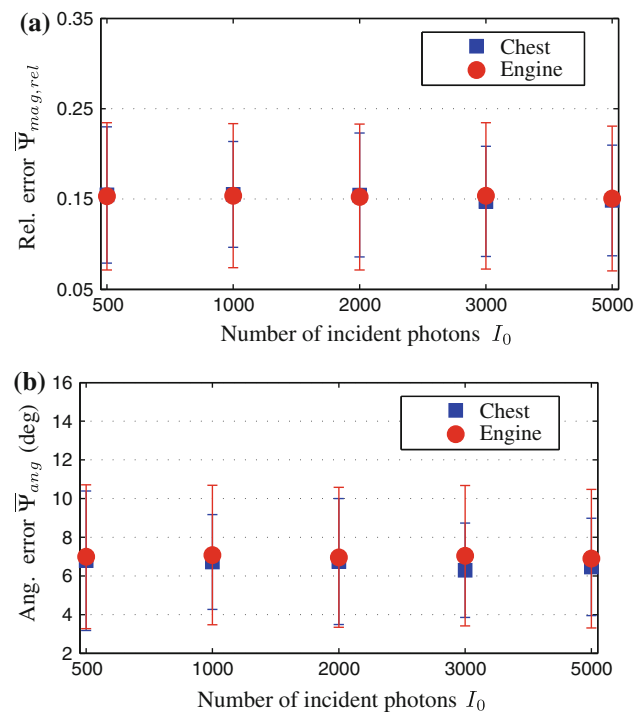


**Fig. 11** Errors for the 3d deformation estimation using the datasets chest and engine with different number of incident photons  $I_0$ . Relative error (a). Angular error in degrees (b). In all plots, the standard deviation is also shown

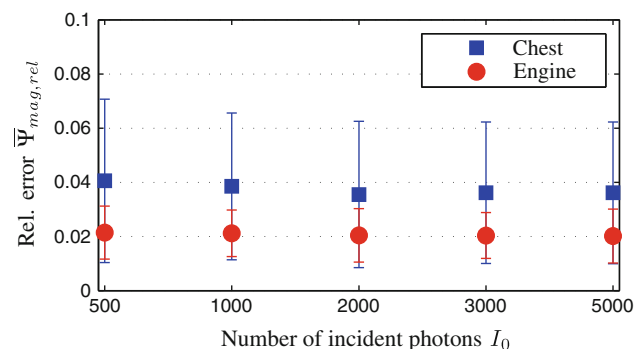


**Fig. 12** Relative error for the deformation estimation using the 3d datasets chest and engine with different  $I_0$ , allowing only six degrees of freedom (translation and scaling). The standard deviation is also shown

Radon transform in Eq. 25) results in an averaging of the noisy projection data, hence the standard deviation (which is a measure of the amount of noise) is reduced. Compared to the 2d results in Fig. 10, the error level is generally higher by a factor of two. This is due to the fact that for the 3d case, 12 unknowns must be fitted in the estimation procedure compared to only 6 in the 2d case. This poses a more difficult problem to the optimization algorithm. To support this explanation, we also tested the engine and chest datasets with only six degrees of freedom, namely translation and scaling. From Fig. 12, we see that consequently the estimation errors are decreased to the level of the 2d estimation problem.

#### 4.4 Reference solution for the experimental data

First we present reference solutions for the experimental datasets. Due to the handling of the samples, we expect two different influence factors causing deformation. First, a rigid body transformation will occur because the sample is dismounted between the scans. Second, the water is expected to induce swelling of the wood. We will see later that the resulting deformation can indeed be very well approximated by an affine model. We compute reference solutions only for the  $2d$  experiments. The manual methods described below are very difficult to apply to a  $3d$  dataset, and automated measures, e.g. normalized cross correlation, are not very meaningful due to the unstable microstructure of the beech sample, cf. Fig. 15.

##### 4.4.1 Reference solutions for the beech samples ( $2d$ )

For each of the two beech samples, we asked two independent operators to identify six pairs of points which do correspond to the same image features. Together with our own estimate of corresponding points, we then have 18 pairs of points which identify corresponding image features. The reference solution is then computed by the use of least squares. This yields our reference solution, which is given by

$$\underline{A}_{\text{beech1}} = \begin{pmatrix} 1.014 & -0.158 \\ 0.183 & 1.109 \end{pmatrix} \quad (42)$$

$$\underline{u}_{\text{beech1}} = \begin{pmatrix} 14.679 \\ 50.551 \end{pmatrix} \quad (43)$$

for the sample “beech1” and

$$\underline{A}_{\text{beech2}} = \begin{pmatrix} 1.008 & -0.164 \\ 0.181 & 1.065 \end{pmatrix} \quad (44)$$

$$\underline{u}_{\text{beech2}} = \begin{pmatrix} 15.800 \\ 51.162 \end{pmatrix} \quad (45)$$

for the sample “beech2”. One sees that the deformations for “beech1” and “beech2” are very similar, even though the  $z$  coordinates are significantly different.

##### 4.4.2 Reference solution for the pine sample

The “pine” sample shows almost no non-rigid deformation (a possible reason for this could be the heat treatment), such that it is easy to identify corresponding points. Again 18 pairs of corresponding points were selected and the associated affine estimate was computed using least squares, yielding

$$\underline{A}_{\text{pine}} = \begin{pmatrix} 1.002 & 0.050 \\ -0.064 & 1.002 \end{pmatrix} \quad (46)$$

$$\underline{u}_{\text{pine}} = \begin{pmatrix} 39.420 \\ -177.340 \end{pmatrix}. \quad (47)$$

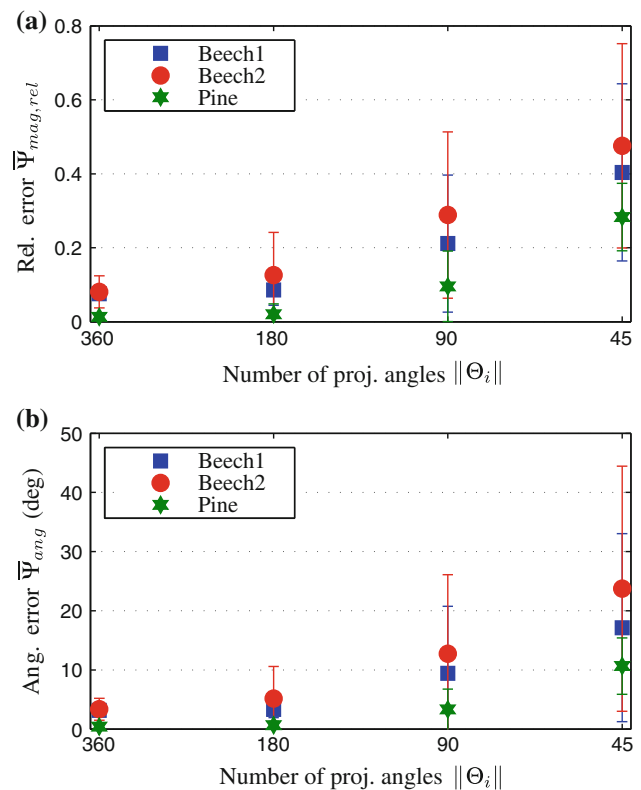


**Fig. 13** Errors for the deformation estimation using the datasets “beech1”, “beech2” and “pine”. Relative error (a). Angular error in degrees (b). In all plots, the standard deviation is also shown

#### 4.5 Results from experimental data

We present deformation estimation results from the experimental data obtained by the procedures described in 4.1.3. From the 1,501 available projections, we use  $\|\Theta_i\| = \{360, 180, 90, 45\}$ ,  $1 \leq i \leq 4$  and set the multiresolution parameter  $L = 5$ , i.e. 6 multiresolution levels. The identity mapping  $\mathbf{T}_{\text{est}}^0(\mathbf{x}) = \mathbf{x}$  was selected as initial estimate for all tests. Again, we compute the standard deviation by the use of cross validation: For each set of projection angles  $\Theta_i$ , we perform the motion estimation by randomly selecting  $\|\Theta_i\|$  angles and repeat this procedure 60 times for each  $\Theta_i$ . The accuracy of the estimated motion is measured using the error measures Eqs. 40 and 41. The results for the  $2d$  estimation are shown in Fig. 13.

The results are in good agreement with the simulated data in Fig. 10 for  $\|\Theta\| \geq 180$ . For smaller numbers of projection angles, the estimation accuracy decreases rapidly. Only the “pine” dataset performs reasonably well even for few projections angles, which is probably due to the simple deformation (almost exclusively translational) and the lack of microstructural change due to water uptake. Also, the random sampling of the projection angles has a strong influence on the estimation accuracy. For example, if 45 equiangular sampled



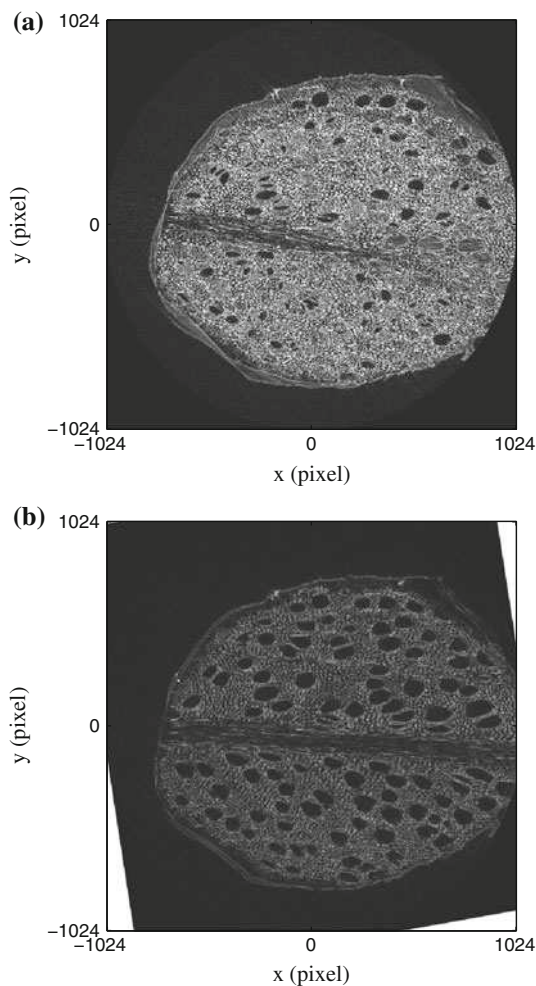


**Fig. 14** Example of a deformation estimation result for the “beech1” dataset. Pointwise absolute difference between the dry state and the wet state, scaled for better visibility (a). Pointwise absolute difference between the dry state deformed with the estimated transformation and the wet state, scaled for better visibility (b). The estimated deformation is  $\underline{A}_{beech1} = \begin{pmatrix} 1.011 & -0.170 \\ 0.181 & 1.100 \end{pmatrix}$ ,  $\underline{u} = \begin{pmatrix} 13.265 \\ 50.060 \end{pmatrix}$ , the relative error is 7.7%. The goodness of the deformation estimation is demonstrated by the proper alignment of the large cells (the tracheids). Also, the growth ring (the horizontal high density region) is properly aligned

projection angles are chosen, the relative error Eq. 40 is 0.245 and 0.346 for the “beech1” and “beech2” datasets, respectively. In Fig. 14, the improvement of the visual correspondence for the dataset “beech1” using the estimated transformation is shown, using 360 projection angles.

As we have no quantitative criteria for the 3d beech dataset, we illustrate the estimation result using the visual correspondence before and after the estimation process. We use  $\|\Theta_1\| = 180$ ,  $\|\Theta_2\| = 40$ , the multiresolution parameter  $L = 5$  and the fraction of used profiles  $k = 0.05$ , cf. Sect. 3.4.1. A good agreement is found between the dry state deformed with the estimated transformation and the wet state, if the alignment of the large cells (the tracheids) and the growth ring is considered, see Figs. 15 and 16.

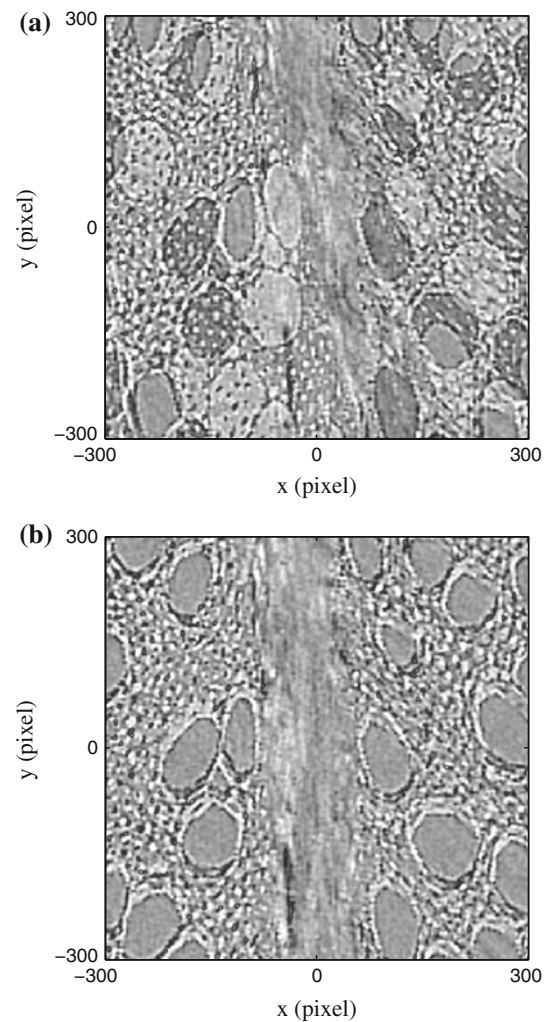


**Fig. 15** Example of a deformation estimation result for the 3d beech dataset. Pointwise absolute difference between the dry state and the wet state at  $z = 200$  (a). Pointwise absolute difference between the dry state deformed with the estimated transformation and the wet state at  $z = 200$  (b). Although the large cells and the growth ring are properly aligned, the microstructure remains misaligned, this prevents the successful use of cross correlation to quantify the alignment

It is worth to notice that a similar estimation approach using the reconstructed image volumes would use a tremendous amount of computational resources: Even if we would only keep the reference and deformed volumes in memory, this alone would need at least  $2 \times 8 \times 200 \times 2,048 \times 2,048 = 12.8$  GB of memory (assuming double precision data). Our approach however needs only about  $2 \times 8 \times 180 \times 40 \times 2,048 = 0.23$  GB of memory for the data. Additionally, also the computational complexity is considerably lower. The standard approach would reconstruct 200 data slices of size  $2,048 \times 2,048$  using 1,501 projection angles for each volume, whereas our approach only computes the Radon transform for 180 projection images of size  $2,048 \times 200$ , using 40 projection angles. This alone results in a speedup of more than  $400\times$ .

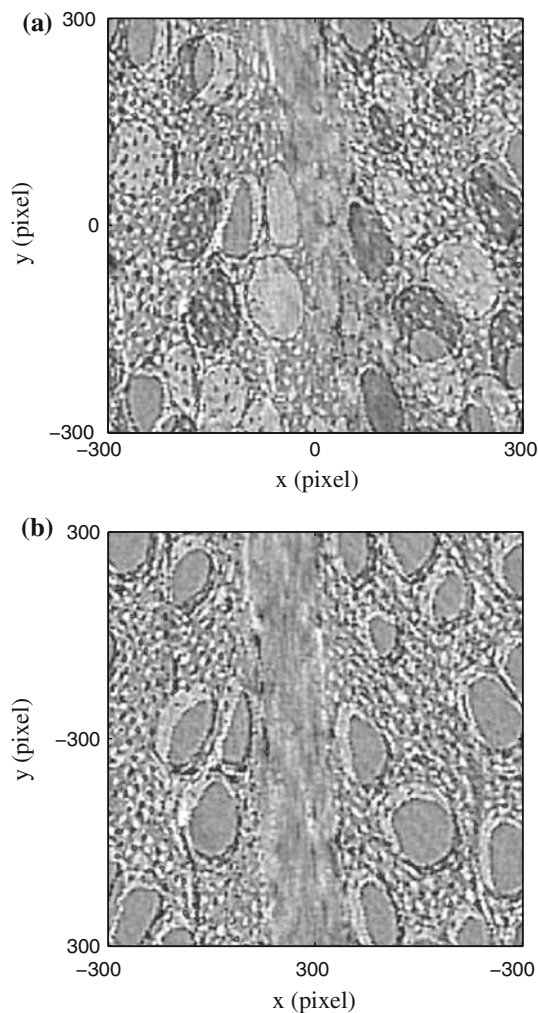


**Fig. 16** Example of a deformation estimation result for the 3d beech dataset. Pointwise absolute difference between the dry state and the wet state at  $z = 50$  (a). Pointwise absolute difference between the dry state deformed with the estimated transformation and the wet state at  $z = 50$  (b)

## 5 Conclusion

We developed an unified approach for two- and three-dimensional projection based affine motion estimation for parallel and fan beam geometries. The approach has been verified using simulated and experimental data. We have shown that it is possible to achieve a mean relative magnitude error of less than 10% for 6 degrees of freedom and less than 15% for 12 degrees of freedom. Besides the progress in theoretical knowledge about motion estimation from tomographic projections, our work provides multiple improvements in practical applications:

- The amount of computational resources needed is drastically reduced. Despite modern multi CPU and GPU reconstruction techniques, especially the enormous memory requirements for high resolution three dimensional

data is still a challenging issue. As shown by the example with the three dimensional beech dataset, our approach uses only a fraction of the memory needed for a full volume reconstruction, thus no special hardware is required.

- The number of projections needed is considerably reduced compared to the standard reconstruction approach. This results in an accelerated scanning time and minimizes the radiation dose delivered to the sample. Especially the radiation dose is often a concern in applications working with biological samples.
- Working directly with projection data minimizes the influence of artifacts which are often present in volume reconstructions. These artifacts are localized in the projection data, but delocalized (i.e. smeared out) in the reconstructed image data. Often, local artifacts have only a limited influence on image processing techniques (e.g. motion estimation), while globally disturbed image/volume data poses a much more difficult problem.
- For the three dimensional case, also the noise reduction due to the averaging effect of the outer Radon transform in Eq. 25 must be mentioned. This makes the proposed approach attractive for scans resulting in projection data with low signal to noise ratio. e.g. due to materials with high X-ray absorption coefficients.

For further research, the choice of the optimization algorithm and the selection of the similarity measure could significantly improve the motion estimation framework.

**Acknowledgments** The authors are grateful to Samuel McDonald from the Swiss Light Source (SLS) at the Paul Scherrer Institute (PSI), Villigen, Switzerland, for his help while performing the synchrotron experiments at the TOMCAT beamline.

## Appendix A: Cone beam geometry

It would be tempting to apply our projection based motion estimation approach to the widely used cone beam geometry. However, there is a fundamental problem due to the *Tuy-Smith* condition [36, 37]. This condition states that the Radon space data is only completely sampled if every plane which intersects the sample also intersects the source trajectory. For the cone beam geometry, only points which belong to the  $xy$ -plane ( $z = 0$ ) satisfy this condition. It is hence not possible to compute the three-dimensional Radon transform from the cone beam projection images. The development of approximate methods for the computation of the three dimensional Radon transform could, however, help to overcome this limitation.

## Appendix B: Computation of the Jacobian for the optimization

We investigate the computation of the Jacobian matrix used to solve Eq. 20 for the 2d case. Let  $\mathbf{t}_a = (t_1, t_2, \dots, t_6)$  be the



parameters of the affine transformation  $\mathbf{T}_a$ . We identify the first four parameters  $t_1, \dots, t_4$  as parameters of the matrix  $\underline{A}_a$  and  $t_5, t_6$  as parameters of the translation  $\mathbf{u}$ , i.e.

$$\underline{A}_a = \begin{pmatrix} t_1 & t_2 \\ t_3 & t_4 \end{pmatrix}, \quad \mathbf{u} = \begin{pmatrix} t_5 \\ t_6 \end{pmatrix}, \quad (48)$$

cf. Eq. 7. The Jacobi matrix is given by

$$\underline{J}_\Psi = \begin{pmatrix} \frac{\partial \Psi(\mathbf{T}_a, \theta_1)}{\partial t_1} & \dots & \frac{\partial \Psi(\mathbf{T}_a, \theta_1)}{\partial t_6} \\ \vdots & & \vdots \\ \frac{\partial \Psi(\mathbf{T}_a, \theta_{\parallel \Theta})}{\partial t_1} & \dots & \frac{\partial \Psi(\mathbf{T}_a, \theta_{\parallel \Theta})}{\partial t_6} \end{pmatrix} \quad (49)$$

and

$$\Psi(\mathbf{T}_a, \theta) = 1 - NCC \left( \check{f}_{\text{ref}} \left( \check{\mathbf{T}}_a(p), \check{\mathbf{T}}_a(\xi_\theta) \right), \check{f}_{\text{def}}(p, \xi_\theta) \right), \quad (50)$$

cf. Eqs. 15 and 17. In order to ease the notation, set

$$\begin{aligned} I_1 &:= \check{f}_{\text{ref}} \left( \check{\mathbf{T}}_a(p), \check{\mathbf{T}}_a(\xi_\theta) \right) \\ I_2 &:= \check{f}_{\text{def}}(p, \xi_\theta), \end{aligned} \quad (51)$$

then

$$\Psi(\mathbf{T}_a, \theta) = 1 - \frac{\sum (I_1 - \bar{I}_1)(I_2 - \bar{I}_2)}{\left( \sum (I_1 - \bar{I}_1)^2 \sum (I_2 - \bar{I}_2)^2 \right)^{\frac{1}{2}}} \quad (52)$$

$$:= 1 - \frac{I_{12}}{\sqrt{I_{11} I_{22}}}. \quad (53)$$

Therefore,

$$\frac{\partial \Psi}{\partial t_i} = - \frac{\sum \left( \frac{\partial I_1}{\partial t_i} - \frac{\partial \bar{I}_1}{\partial t_i} \right) (I_{11}(I_2 - \bar{I}_2) - I_{12}(I_1 - \bar{I}_1))}{I_{11} \sqrt{I_{11} I_{22}}}, \quad (54)$$

for  $i = 1, \dots, 6$ . To evaluate the derivatives of the type  $\frac{\partial I_1}{\partial t_i}$ , we need the spline interpolation as discussed in Sect. 3.3.1. Let  $b_{k,l}$  be the spline coefficients and  $B_k^3(p)$  and  $B_l^3(\theta)$  be the cubic spline basis functions. Then, in the  $(p, \theta)$  coordinate system with transformation  $\check{\mathbf{T}}_a$ ,  $I_1$  is given by

$$I_1(\check{\mathbf{T}}_a(p), \check{\mathbf{T}}_a(\theta)) = \sum_{k,l} b_{k,l} B_k^3(\check{\mathbf{T}}_a(p)) B_l^3(\check{\mathbf{T}}_a(\theta)) \quad (55)$$

with

$$\check{\mathbf{T}}_a(p) = \frac{p + \langle \underline{A}_a^{-\top} \xi_\theta, \mathbf{u} \rangle}{\| \underline{A}_a^{-\top} \xi_\theta \|} \quad (56)$$

$$\check{\mathbf{T}}_a(\theta) = \theta + \arccos \left( \frac{\langle \xi_\theta, \underline{A}_a^{-\top} \xi_\theta \rangle}{\| \underline{A}_a^{-\top} \xi_\theta \|} \right) \quad (57)$$

cf. Eqs. 11 and 12. It follows that

$$\begin{aligned} \frac{\partial I_1}{\partial t_i} &= \sum_{k,l} b_{k,l} \left( \frac{\partial \check{\mathbf{T}}_a(p)}{\partial t_i} B_k^{'3}(\check{\mathbf{T}}_a(p)) B_l^3(\check{\mathbf{T}}_a(\theta)) \right. \\ &\quad \left. + \frac{\partial \check{\mathbf{T}}_a(\theta)}{\partial t_i} B_l^{'3}(\check{\mathbf{T}}_a(\theta)) B_k^3(\check{\mathbf{T}}_a(p)) \right), \end{aligned} \quad (58)$$

where  $B_k^{'3}$  and  $B_l^{'3}$  denote the outer derivatives of  $B_k^3(\check{\mathbf{T}}_a(p))$  and  $B_l^3(\check{\mathbf{T}}_a(\theta))$ , respectively. These outer derivatives can easily be computed because the basis functions are polynomials.

It remains to compute  $\frac{\partial \check{\mathbf{T}}_a(p)}{\partial t_i}$  and  $\frac{\partial \check{\mathbf{T}}_a(\theta)}{\partial t_i}$ . For  $i = 5, 6$  (i.e. the translational part of  $\check{\mathbf{T}}_a$ ), it immediately follows that

$$\begin{aligned} \frac{\partial \check{\mathbf{T}}_a(p)}{\partial t_5} &= \frac{\left\langle \underline{A}_a^{-\top} \xi_\theta, \begin{pmatrix} 1 \\ 0 \end{pmatrix} \right\rangle}{\| \underline{A}_a^{-\top} \xi_\theta \|}, \quad \frac{\partial \check{\mathbf{T}}_a(\theta)}{\partial t_5} = 0 \\ \frac{\partial \check{\mathbf{T}}_a(p)}{\partial t_6} &= \frac{\left\langle \underline{A}_a^{-\top} \xi_\theta, \begin{pmatrix} 0 \\ 1 \end{pmatrix} \right\rangle}{\| \underline{A}_a^{-\top} \xi_\theta \|}, \quad \frac{\partial \check{\mathbf{T}}_a(\theta)}{\partial t_6} = 0. \end{aligned} \quad (59)$$

For the derivatives w.r.t.  $t_i$ ,  $i = 1, \dots, 4$ , we fix the following notation:

$$\underline{A}_{\xi_\theta} := \underline{A}^{-\top} \xi_\theta, \quad \underline{A}_{\partial_i} := \frac{\partial \underline{A}}{\partial t_i}. \quad (60)$$

Then,

$$\begin{aligned} \frac{\partial \check{\mathbf{T}}_a(p)}{\partial t_i} &= \frac{1}{\| \underline{A}_{\xi_\theta} \|^2} \left[ \xi_\theta^\top \underline{A}_{\partial_i}^{-1} \mathbf{u} \| \underline{A}_{\xi_\theta} \| - (\langle \underline{A}_{\xi_\theta}, \mathbf{u} \rangle + p) \right. \\ &\quad \left. \times \frac{1}{2 \| \underline{A}_{\xi_\theta} \|} \xi_\theta^\top \left( \underline{A}_{\partial_i}^{-1} \underline{A}^{-\top} + \underline{A}^{-1} \underline{A}_{\partial_i}^{-\top} \xi_\theta \right) \xi_\theta \right], \end{aligned} \quad (61)$$

for  $i = 1, \dots, 4$ . Likewise,

$$\begin{aligned} \frac{\partial \check{\mathbf{T}}_a(\theta)}{\partial t_i} &= - \frac{1}{\sqrt{1 - \frac{\langle \xi_\theta, \underline{A}_{\xi_\theta} \rangle^2}{\| \underline{A}_{\xi_\theta} \|^2}}} \left[ \frac{1}{\| \underline{A}_{\xi_\theta} \|^2} \left( \xi_\theta^\top \underline{A}_{\partial_i}^{-1} \xi_\theta \| \underline{A}_{\xi_\theta} \| \right. \right. \\ &\quad \left. \left. - \xi_\theta^\top \underline{A}^{-\top} \xi_\theta \frac{1}{2 \| \underline{A}_{\xi_\theta} \|} \xi_\theta^\top \left( \underline{A}_{\partial_i}^{-1} \underline{A}^{-\top} + \underline{A}^{-1} \underline{A}_{\partial_i}^{-\top} \right) \xi_\theta \right) \right], \end{aligned} \quad (62)$$

for  $i = 1, \dots, 4$ . Note that

$$\frac{\partial \underline{A}^{-1}}{\partial t_i} = - \underline{A}^{-1} \frac{\partial \underline{A}}{\partial t_i} \underline{A}^{-1}, \quad (63)$$

hence all expressions in Eqs. 61 and 62 are directly computable.

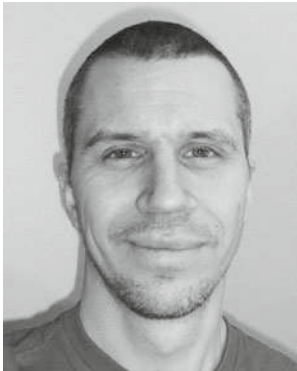
## References

- Geers, M.G.D., DeBorst, R., Brekelmans, W.A.M.: Computing strain fields from discrete displacement fields in 2d-solids. *Int. J. Solids Struct.* **33**(29), 4293–4307 (1996)
- Bay, B., Smith, T., Fyhrie, D., Saad, M.: Digital volume correlation: three-dimensional strain mapping using X-ray tomography. *Exp. Mech.* **39**(3), 217–226 (1999)
- Verhulp, E., Rietbergen, B. van, Huijskes, R.: A three-dimensional digital image correlation technique for strain measurements in microstructures. *J. Biomech.* **37**(9), 1313–1320 (2004)
- Zhang, D., Zhang, X., Cheng, G.: Compression strain measurement by digital speckle correlation. *Exp. Mech.* **39**(1), 62–65 (1999)
- Cheng, P., Sutton, M., Schreier, H., McNeill, S.: Full-field speckle pattern image correlation with b-spline deformation function. *Exp. Mech.* **42**(3), 344–352 (2002)
- Maintz, J.B., Viergever, M.A.: A survey of medical image registration. *Med. Image Anal.* **2**(1), 1–36 (1998)
- Zitova, B., Flusser, J.: Image registration methods: a survey. *Image Vis. Comput.* **21**(11), 977–1000 (2003)
- Natterer, F., Wuebbeling, F.: Mathematical methods in image reconstruction. *Soc. Ind. Appl. Math. Philadelphia* (2001)
- Kak, A.C., Slaney, M.: Principles of Computerized Tomographic Imaging. IEEE Press, New York (1988)
- De Man, B., Nuyts, J., Dupont, P., Marchal, G., Suetens, P.: Reduction of metal streak artifacts in X-ray computed tomography using a transmission maximum a posteriori algorithm. *IEEE Trans. Nuclear Sci.* **47**(3), 977–981 (2000)
- Fitchard, E.E., Aldridge, J.S., Reckwerdt, P.J., Mackie, T.R.: Registration of synthetic tomographic projection data sets using cross-correlation. *Phys. Med. Biol.* **43**(6), 1645–1657 (1998)
- Fitchard, E.E., Aldridge, J.S., Reckwerdt, P.J., Olivera, G.H., Mackie, T.R., Iosevich, A.: Six parameter patient registration directly from projection data. *Nuclear Instrum. Methods Phys. Res. Sect. a-Accelerators Spectrom. Detect. Assoc. Equip.* **421**(1–2), 342–351 (1999)
- Fitchard, E.E., Aldridge, J.S., Ruchala, K., Fang, G., Balog, J., Pearson, D.W., Olivera, G.H., Schloesser, E.A., Wenman, D., Reckwerdt, P.J., Mackie, T.R.: Registration using tomographic projection files. *Phys. Med. Biol.* **44**(2), 495–507 (1999)
- Lu, W.G., Fitchard, E.E., Olivera, G.H., You, J., Ruchala, K.J., Aldridge, J.S., Mackie, T.R.: Image/patient registration from (partial) projection data by the fourier phase matching method. *Phys. Med. Biol.* **44**(8), 2029–2048 (1999)
- Bingham, P., Arrowood, L.: Projection registration applied to non-destructive testing. *J. Electron. Imag.* **19**(3) (2010)
- Weihs, M., Tianfang, L., Nicole, W., Lei, X.: Ct image registration in sinogram space. *Med. Phys.* **34**(9), 3596–3602 (2007)
- Milanfar, P.: A model of the effect of image motion in the radon transform domain. *IEEE Trans. Image Process.* **8**(9), 1276–1281 (1999)
- Robinson, D., Milanfar, P.: Fast local and global projection-based methods for affine motion estimation. *J. Math. Imag. Vis.* **18**(1), 35–54 (2003)
- Desbat, L., Roux, S., Grangeat, P.: Compensation of some time dependent deformations in tomography. *IEEE Trans. Med. Imag.* **26**(2), 261–269 (2007)
- Bartels, C., de Haan, G.: Direct motion estimation in the radon transform domain using match-profile backprojections. In: de Haan, G. (ed.) *Image Processing, 2007. ICIP 2007. IEEE International Conference on*, vol. 6, pp. VI-153–VI-156 (2007)
- Tatsuhiko, T., Shinichi, H.: Detection of planar motion objects using radon transform and one-dimensional phase-only matched filtering. *Syst. Comput. Jpn.* **37**(5), 56–66 (2006)
- Traver, J.V., Pla, F.: Motion analysis with the radon transform on log-polar images. *J. Math. Imag. Vis.* **30**(2), 147–165 (2008)
- Mooser, R., Hack, E., Sennhauser, U., Székely, G.: Estimation of affine transformations directly from tomographic projections. In: *6th International Symposium on Image and Signal Processing and Analysis*, pp. 377–382. Salzburg, Austria (2009)
- Deans, S.R.: *The Radon Transform and Some of its Applications*. Wiley, New York (1983)
- Woods, R.P.: Spatial transformation models. In: *Handbook of medical imaging*, pp. 465–490. Academic Press, Inc., San Diego (2000)
- Lewis, J.P.: Fast normalized cross-correlation. In: *Vision Interface*, pp. 120–123. Canadian Image Processing and Pattern Recognition Society (1995)
- Richard, H.B., Robert, B.S., Gerald, A.S.: Approximate solution of the trust region problem by minimization over two-dimensional subspaces. *Math. Program.* **40**(3), 247–263 (1988)
- De Boor, C.: *A Practical Guide to Splines*, rev. edn. Springer, New York (2001)
- Lindeberg, T.: Scale-space theory: A basic tool for analysing structures at different scales. *J. Appl. Stat.* **21**(2), 224–270 (1994)
- Forsberg, F., Mooser, R., Arnold, M., Hack, E., Wyss, P.: 3d micro-scale deformations of wood in bending: synchrotron radiation [mu]ct data analyzed with digital volume correlation. *J. Struct. Biol.* **164**(3), 255–262 (2008)
- Forsberg, F., Sjö Dahl, M., Mooser, R., Hack, E., Wyss, P.: Full three-dimensional strain measurements on wood exposed to three-point bending: Analysis by use of digital volume correlation applied to synchrotron radiation micro-computed tomography image data. *Strain* **46**(1), 47–60 (2010)
- Trtik, P., Dual, J., Keunecke, D., Mannes, D., Niemz, P., Stähli, P., Kaestner, A., Groso, A., Stampanoni, M.: 3d imaging of micro-structure of spruce wood. *J. Struct. Biol.* **159**(1), 46–55 (2007)
- Marone, F., Hintermüller, C., McDonald, S., Abela, R., Mikuljan, G., Isenegger, A., Stampanoni, M.: X-ray tomographic microscopy at tomcat. In: *Developments in X-Ray Tomography VI*, vol. 7078, pp. 707,822–11. SPIE, San Diego (2008)
- Stampanoni, M., Groso, A., Isenegger, A., Mikuljan, G., Chen, Q., Meister, D., Lange, M., Betemps, R., Henein, S., Abela, R.: Tomcat: A beamline for TOMographic Microscopy and Coherent rADIology experiments. *AIP Conf. Proceed.* **879**(1), 848–851 (2007)
- Schretter, C., Neukirchen, C., Bertram, M., Rose, G.: Correction of some time-dependent deformations in parallel-beam computed tomography. In: *Biomedical Imaging: From Nano to Macro, 2008. ISBI 2008. 5th IEEE International Symposium on*, pp. 764–767 (2008)
- Tuy, H.K.: An inversion-formula for cone-beam reconstruction. *Siam J. Appl. Math.* **43**(3), 546–552 (1983)
- Smith, B.D.: Image reconstruction from cone-beam projections: Necessary and sufficient conditions and reconstruction methods. *IEEE Trans. Med. Imag.* **4**(1), 14–25 (1985)

## Author Biographies



**René Mooser** received his diploma degree in Computational Science and Engineering in 2006 and a Ph.D. degree from the Swiss Federal Institute of Technology (ETH), Zurich, Switzerland, in 2010. While pursuing his Ph.D. degree, he was an assistant researcher at the Swiss Federal Laboratories for Materials Testing and Research (EMPA) in the fields of computed tomography and image processing. Currently, he is working in the financial industry, developing algorithmic trading strategies.



**Fredrik Forsberg** received his Masters degree in Engineering Physics in 2002 and his Ph.D. in Experimental Mechanics from Luleå University of Technology, Luleå, Sweden, in 2008. He is currently a researcher at LKAB R&D, Luleå, Sweden. His main areas of research are X-ray microtomography, correlation based techniques and 2D/3D image analysis.

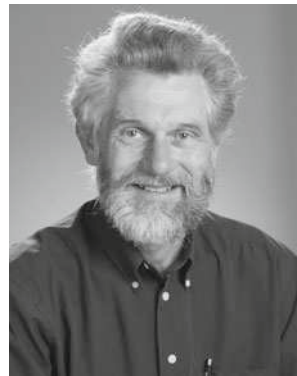


**Erwin Hack** received the diploma degree in theoretical physics and a Ph.D. degree in physical chemistry from the University of Zurich, Switzerland, in 1986 and 1991, respectively. He is a senior scientist at the Swiss Federal Laboratories for Materials Testing and Research (Empa), where he is working on full-field optical measurement techniques. His research interests are interferometry, infrared imaging and image analysis. He has authored and co-authored 23 papers in peer-reviewed journals and more than 25 conference papers. He is a member of the Editorial Board of *Optics and Lasers in Engineering* (Elsevier), the European Optical Society and the Optical Society of America.



alization, and simulation methods for computer support of medical diagnosis, therapy, training, and education.

**Gábor Székely** received his degree in chemical engineering from the Technical University of Budapest in 1974, and a degree in applied mathematics from the University of Budapest in 1981. He also obtained his Ph.D. degree in analytical chemistry from the Technical University of Budapest in 1985. Currently, he is a professor of medical image analysis and visualization at the Computer Vision Laboratory of ETH Zurich and is developing image analysis, visu-



**Urs Sennhauser** received his Ph.D. degree in Physics from the Swiss Federal Institute of Technology (ETH), Zurich, Switzerland, in 1981. He is heading the Electronics/Metrology Laboratory and the Reliability Center at the Swiss Federal Laboratories for Materials Testing and Research (Empa). He is currently lecturing “Reliability of Devices and Systems” and “Physics of Failure and Failure Analysis of Electronic Circuits and Devices” at ETH Zurich. In addition to national affiliations, he is an active member of international professional organizations such as IEEE, APS and SPIE.